Operando spectroscopic investigation of the valence change mechanism in La_2NiO_4+δ−basedmemristivedevices

Thoai-khanh Khuu, Aleksandra Koroleva, Carlos Moncasi, Alexander Stangl, David Cooper, Gauthier Lefèvre, Fabrice Wilhelm, Andrei Rogalev, Matthieu Weber, Carmen Jiménez, et al.

ADVANCED ELECTRONIC MATERIALS Open Access
www.advelectronicmat.de

Operando Spectroscopic Investigation of the Valence Change Mechanism in $La_2NiO_{4+\delta}$ -Based Memristive Devices

*Thoai-Khanh Khuu, Aleksandra Koroleva, Carlos Moncasi, Alexander Stangl, David Cooper, Gauthier Lefèvre, Fabrice Wilhelm, Andrei Rogalev, Matthieu Weber, Carmen Jiménez, and Mónica Burriel**

Valence change memory devices, based on redox reactions and oxygen dynamics, are considered to be one of the most promising candidates for the next generation of non-volatile memory devices and neuromorphic architectures. Devices based on $La_2NiO_{4+\delta}$ have demonstrated analog resistive switching behavior, but the underlying mechanism is not fully understood. To get a profound understanding of the device's behavior, the employment of element-selective techniques to provide direct information on oxygen migration is of paramount importance. In this work, $TiN/La_2NiO_{4+\delta}/Pt$ devices are studied using an original operando X-ray absorption near edge spectroscopy (XANES) methodology based on monitoring absorbance intensity changes at a fixed energy position which, in combination with in situ electron energy-loss spectroscopy (EELS) measurements, has provided valuable insights into the resistive switching mechanism. This approach allows to study the formation of the TiN_xO_y interlayer at the $TiN/La_2NiO_{4+\delta}$ interface and directly monitor oxygen migration between TiN_xO_y and $La_2NiO_{4+\delta}$. An energy shift of the Ni K-edge spectra is consistently measured during the device operation as it underwent cycling in both voltage polarities, thus confirming the pivotal role of the valence change mechanism in the resistive switching behavior of these devices. Furthermore, a switching model based on the coexistence of filamentary and interfacial switching is proposed.

1. Introduction

Resistive switching (RS) devices, also known as memristive devices, are one of the promising candidates for the next generation of memories because of their simple metal/insulator/metal structure, scalability, potential complementary metal-oxide-semiconductor (CMOS) compatibility, high speed, and low energy consumption.[1] The key property of a memristive device is the ability to change its resistance under an applied electric field, which gives rise to various possible applications, from non-volatile resistive random access memories (RRAM)[2] to neuromorphic architectures.[3–6] Extensively researched in the past years, the memristive phenomenon was shown in various materials: transition metal oxides,[7,8] perovskites,[9,10] organic compounds,[11–13] etc. Particularly, perovskites and related oxides such as $SrTiO_3$,[14–18] $LaMnO_{3+\delta}$,[19–21] $(La,Sr)MnO_3$,[22,23] $Pr_{0.7}Ca_{0.3}MnO_3$

T.-K. Khuu, A. Koroleva, C. Moncasi, A. Stangl, M. Weber, C. Jiménez, M. Burriel
Université Grenoble Alpes
CNRS
Grenoble INP
LMGP
Grenoble 38000, France
E-mail: monica.burriel@grenoble-inp.fr

The ORCID identification number(s) for the author(s) of this article can be found under https://doi.org/10.1002/aelm.202400313

DOI: 10.1002/aelm.202400313

T.-K. Khuu, G. Lefèvre
Université Grenoble Alpes
CNRS
CEA/LETI Minatec
LTM
Grenoble 38000, France

A. Koroleva
Université Grenoble Alpes
CNRS
Grenoble INP
TIMA
Grenoble 38000, France

D. Cooper
Université Grenoble Alpes
CEA-LETI
Grenoble 38000, France

F. Wilhelm, A. Rogalev
European Synchrotron Radiation Facility (ESRF)
Grenoble F-38054, France

(PCMO),[24–27] or $La_2NiO_{4+\delta}$[28–31] drew attention as resistive switching materials because of their tunable electronic and ionic transport properties with a potential for analog behavior, making them promising candidates for neuromorphic devices. Among other materials, and contrary to the most common memristive oxides, which are primarily oxygen deficient, $La_2NiO_{4+\delta}$ (L2NO4) exhibits oxygen storage capabilities along with high oxygen mobility through the presence of highly mobile interstitial oxygen ions, giving rise to mixed ionic-electronic conductivity (MIEC). Using one inert (Pt) and one chemically active electrode (Ti or TiN), due to the oxygen surplus in L2NO4 films it is possible to achieve the formation of a nonstoichiometric TiO_x (TiO_xN_y) layer at the metal/oxide interface, which plays a major role in the RS process.[29,31] Previous studies on the RS behavior in L2NO4 showed multilevel switching with potentiation/depression characteristics,[29,31] stable retention,[28,31] and the ability to control the RS behavior by varying the oxygen content in the film.[30] However, despite the promising results on the initial characterization of RS in L2NO4-based devices, a clear explanation of the RS mechanism underlying the observed behavior is still lacking.

Depending on the materials chosen for the active material and electrodes, the RS process is most often based on the formation of a conductive bridge consisting of metal ions, conductive filaments consisting of oxygen vacancies, or oxygen migration over the device's total area.[32] Consequently, the properties of the device can vary drastically depending on the RS mechanism, which makes the study of the physics of the RS process a crucial task. In addition, the aforementioned mechanisms can coexist in the device,[18,33,34] further compounding the challenge of comprehending the RS mechanisms. In this regard, substantial efforts were taken to model the device's behavior using complex computational models, for example, ab initio modeling or density functional theory (DFT) calculations for HfO_2, TiO_2, Al_2O_3, etc.[35–39] At the same time, the need for experimental proof of the modeling-based hypotheses led to the development of methods that allow probing the device on the atomic scale, as well as conducting in situ and operando measurements to observe the changes in the chemistry of the device directly during the RS process.[40,41] Among other techniques, transmission electron microscopy (TEM) comes as an especially attractive choice due to the opportunity to study the device with atomic-scale resolution.[41] For example, this method was previously used for the observation of conductive bridges of Au,[42] Ag,[43] or Ta[44] ions, conductive filaments in TiO_2,[45,46] or interface chemistry changes in PCMO.[47] At the same time, the observation of the changes in the device's chemistry can be difficult without complementary techniques such as energy-dispersive X-ray (EDX) spectroscopy[48] or electron energy-loss spectroscopy (EELS). For example, Cooper et al. used EELS to study the difference in the oxygen distribution between HRS and LRS in $SrTiO_3$, observing oxygen deficiency at the Pt/$SrTiO_3$ interface in the LRS state.[49]

X-ray absorption near edge spectroscopy (XANES) is another powerful method for the investigation of the RS mechanism since it is an intrinsically element-selective technique, highly sensitive to the oxidation state of the absorbing atom. Previously, the XANES technique was used to investigate the crystalline structure and the chemistry of several materials used for memristive devices. For example, Shih et al. used XANES measurements to study the RS behavior of Cu nanowires, comparing the chemical state of Cu in the HRS and LRS and revealing the current-induced oxidation of the metallic nanowire.[50] Next, Lenser et al. investigated the oxygen vacancy distribution in Fe-$SrTiO_3$ before and after the forming process using micro-focused XANES.[51] Janousch et al. also used this method to study the RS mechanism in a Cr-doped $SrTiO_3$ single-crystal memory.[52] However, in all these cases, the XANES technique was used *ex situ*, which does not show the full picture of the processes underlying the RS behavior. We believe that paired with electrical stimulation (i.e., conducted in operando), XANES measurements can provide valuable information on oxygen migration during the RS process. Operando X-ray absorption spectroscopy measurements were previously used to examine the catalytic activity of enzymes depending on the electrochemical potential.[53] However, to the best of our knowledge, it is yet to be applied to the study of memristive devices. In addition, full-edge measurements are rather time-consuming, so to track the rapid changes in the device chemistry under the application of the external bias, a new specific operando XANES methodology needs to be developed.

In this work, we thoroughly investigate the RS mechanism of TiN/L2NO4/Pt devices using an original operando XANES methodology based on monitoring absorbance intensity changes at a fixed energy position. Our results show that using this non-destructive technique, it is possible to follow in real time the changes in the oxygen stoichiometry in the bulk of the device and get valuable information on the device chemistry changes in the film under external electric bias. In addition, we combined operando XANES measurements with in situ TEM and EELS measurements, which allowed us to gain an understanding of oxygen migration during the RS process by tracking changes in the oxidation states of the N, O, and Ti ions within the TiN/L2NO4/Pt device. These complementary findings, obtained through in situ and operando methodologies, confirmed oxygen drift occurring between the TiN electrode and the L2NO4 layer. Building upon this experimental evidence, we propose a model of the resistive switching mechanism in TiN/L2NO4/Pt memristive devices.

2. Results and Discussion

Figure 1 shows the typical RS behavior of a TiN/L2NO4/Pt memristive device. When the first positive bias is applied, the device is in an intermediate (initial) resistance state (IRS) with a resistance value of ≈23 kΩ. Next, the TiN/L2NO4/Pt device is electrically stressed under bipolar voltage sweeps (0 V → $+V_{max}$ → 0 V → $-V_{max}$ → 0 V). Figure 1a shows five *I-V* curves consecutively measured at $|V_{max}| = 2$ V. Although a small RS hysteresis can be observed, the HRS/LRS ratio is rather small (<5). In addition, under these biasing conditions, the HRS and LRS resistance values depend on the device's area (Figure S1a, Supporting Information), which is often attributed to interfacial, or areal switching. Furthermore, when the $|V_{max}|$ is increased, a sudden increase in current occurs at negative polarity, reaching current compliance (CC) (Figure 1b). This process resembles the classic forming step observed in filamentary RS systems.[54] However, it was previously referred to as a "soft-forming" process due to a

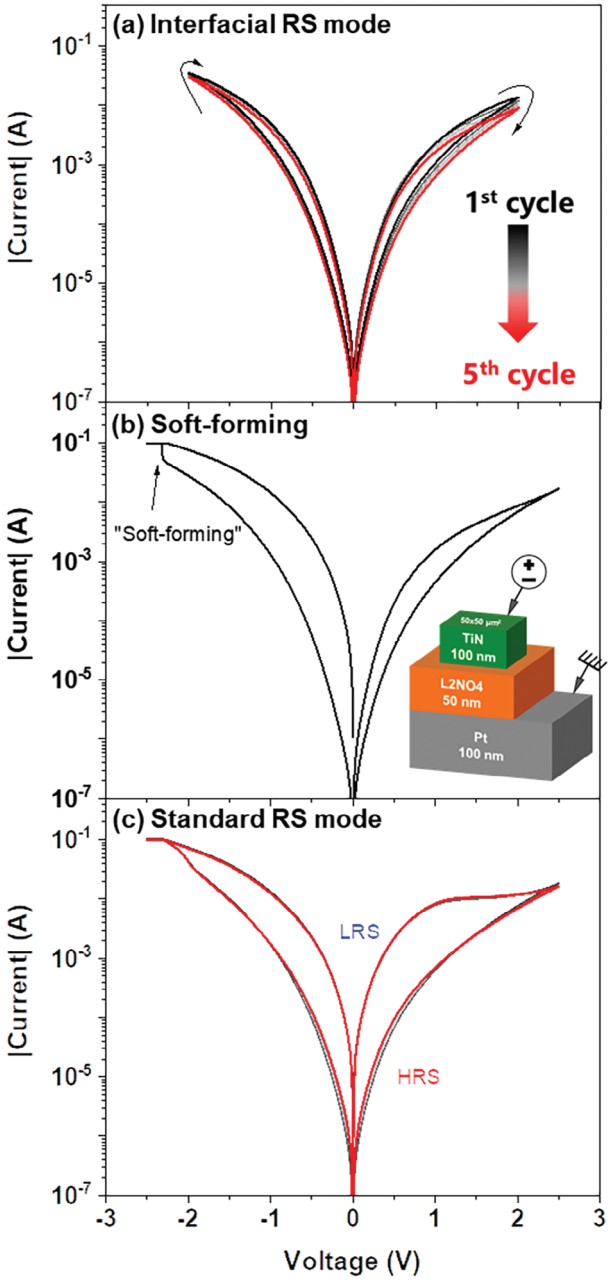

Figure 1. *I–V* characteristics of a TiN/L2NO4/Pt device during the initialization process. The cycles are performed following the same sequence (0 V → $+V_{max}$ → 0 V → $-V_{max}$ → 0 V): a) $|V_{max}| = 2$ V; b) first cycle at $|V_{max}| = 2.5$ V; c) five subsequent cycles at $|V_{max}| = 2.5$ V. Corresponding R–V curves are presented in Figure S3 (Supporting Information).

number of specific differences such as a lack of current overshoot and small but rapid change in current.[31] Figure 1c presents five sweeps at $|V_{max}| = 2.5$ V, showing a reproducible RS behavior with an HRS/LRS ratio of ~36 ($V_{READ} = 0.1$ V) after the "soft-forming". In both polarities, gradual transitions between HRS and LRS can be observed, showing that counter-eightwise analog RS can be obtained on TiN/L2NO4/Pt memristive devices, which is consistent with previous studies.[31] In addition, the curves are slightly asymmetric with a self-compliance region at positive polarity. The presence of the "soft-forming" step suggests that a conductive filament (CF) could be created in the device (filamentary RS mechanism). Another indication of the presence of a CF is the independence of HRS and LRS from the device's area after "soft-forming" (Figure S1b, Supporting Information). Interestingly, if the $|V_{max}|$ and/or CC are carefully controlled, the "soft-forming" can be avoided and the device can work in a purely interfacial mode (Figure S2, Supporting Information). In addition, the device-to-device variability of forming voltage during the "soft-forming" process is shown in Figure S2b (Supporting Information). To make it easier to distinguish between two RS modes, hereafter we will address the behavior observed in Figure 1a as "interfacial RS mode", and the behavior observed in Figure 1c as "standard RS mode". In other RS systems, gradual SET and RESET processes often indicate an interface-type RS mechanism.[24,55,56] However, gradual changes can be also obtained in filamentary RS if the switching is based, for example, on the modulation of the CF size/composition[57,58] or the formation and rupture of multiple CFs.[59,60] Thus, further evidence is needed to unravel the mechanism underlying the RS in the TiN/L2NO4/Pt devices.

To gain an insight into the RS mechanism of the TiN/L2NO4/Pt devices, a study of the conduction mechanism in the device was performed. The most common conduction mechanisms observed in the RS materials include Poole–Frenkel emission, Schottky emission, various tunneling mechanisms (trap-assisted tunneling, direct tunneling, Fowler-Nordheim quantum), and space-charge-limited-current (SCLC) conduction.[61] The isothermal *I–V* correlation can be used to distinguish between the aforementioned mechanisms by fitting the *I-V* curve in the coordinates corresponding to the particular conduction mechanism. The fitting can then be verified by the calculation of the dielectric permittivity from the slope of the fitted curve and comparing it to the high frequency or optical dielectric constant. For L2NO4 an optical dielectric constant of $\varepsilon_{L2NO4} = n_{L2NO4}{}^2 \approx 6.3$ was measured by spectroscopic ellipsometry (fitting results are shown in Figure S4, Supporting Information). It should also be noted that after the TiN deposition, the formation of a TiN_xO_y interlayer of ≈3 nm thickness occurs at the TiN/L2NO4 interface.[31] Therefore, the contribution of this layer should also be taken into account during the dielectric constant calculations. According to the literature, the refractive index of TiN_xO_y can vary in the range of 1.5 – 2.5 depending on the oxygen content,[62] which is difficult to determine in our case since the layer is very thin. Therefore, the dielectric permittivity of the TiN_xO_y layer should be in the range of ε_{TiNxOy} ϵ [2.25; 6.25]. Taking the aforementioned approach, we analyzed the *I-V* curves in Figure 1c and were able to rule out the tunneling mechanisms, as we do not observe a linear relationship in the $ln(|I|/V^2)$ versus $1/|V|$ coordinates for the Fowler-Nordheim tunneling or in the $ln(|I|)$ versus $1/|V|$ coordinates for trap-assisted tunneling, plus the thickness of L2NO4 layer is rather large (≈33 nm). Next, we also discarded the Schottky emission since the estimated dielectric constant of ε ≈ 0.85 is very small compared to TiN_xO_y and L2NO4. At the same time, the fitting in $ln(I/V)$ versus $V^{0.5}$ corresponding to the Poole–Frenkel (P-F) emission showed a linear relationship in HRS at negative polarity with the estimated dielectric constant of ε ≈ 5.6. However, in LRS for both polarities and in HRS at

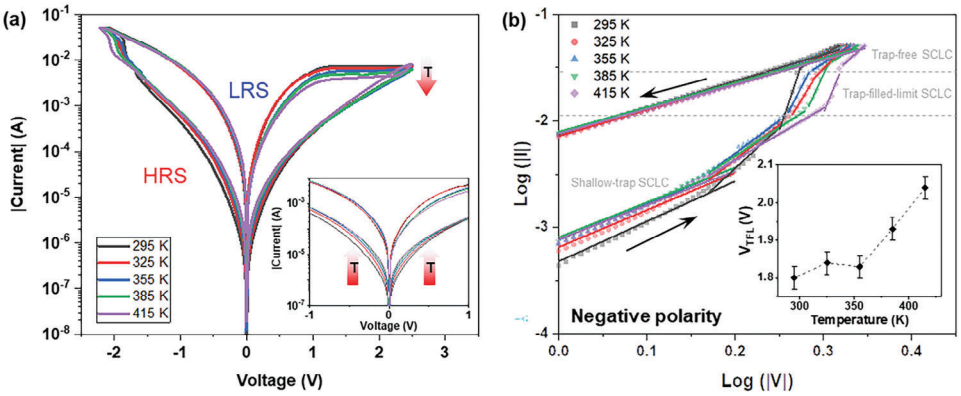

Figure 2. a) *I-V* characteristics of a TiN/L2NO4/Pt device measured at five different temperatures starting from RT (295 K) with an increment of 30 K. The inset shows an expanded view of the low voltage region. b) *I–V* characteristics from Figure 2a plotted in *log(|I|)* versus *log(|V|)* coordinates at negative polarity for the high voltage region. The inset shows the trap-filled-limit voltage (V_{TFL}) as a function of temperature.

positive polarity, a large value of $\varepsilon \approx 13$–15 was obtained, which means that the P-F emission cannot unambiguously explain the conduction mechanism in TiN/L2NO4/Pt devices.

L2NO4 is a *p*-type semiconductor, where the negatively charged O^{2-} ions can be viewed as acceptor dopants, which cause the formation of positively charged holes to maintain charge neutrality in the lattice.[63] Thus, the excess O^{2-} ions can also act as traps for holes during carrier transport through the film, which can gradually fill with carriers under the external bias, resulting in trap-controlled SCLC.[64,65] According to the different models, the traps can be either localized at the single level of shallow trap site in the bandgap or energetically distributed according to an exponential function.[66] In the SCLC model, the α coefficient in the $I \sim V^{\alpha}$ power law dependence changes with the increase of the applied voltage amplitude. Zhang et al. separated the evolution of the $I \sim V^{\alpha}$ power-law dependence for SCLC in solids into four different regions as follows: the low-bias Ohmic regime ($I \sim V$), shallow-trap SCLC ($I \sim V^2$), trap-filled-limit SCLC ($I \sim V^{\alpha}$ with $\alpha > 2$), and finally, trap-free SCLC at sufficiently high bias voltage such that the trap states are completely filled and no longer affect the current conduction ($I \sim V^{\beta}$ with $\beta < \alpha$).[67]

To analyze the possibility of a SCLC mechanism in the case of TiN/L2NO4/Pt devices, we conducted a thorough analysis of the *I–V* curves presented in Figure 1c (details of the fitting can be found in Figure S5, Supporting Information). We observed that the changes in the slope of the curves both in negative and positive polarity are in good agreement with the SCLC model described above, with a transition from the Ohmic behavior at low voltages to a gradual increase in the slope with the voltage increase corresponding to the filling of the exponentially distributed shallow traps in the band gap of L2NO4. In addition, to get a deeper understanding of the observed effects, we conducted a temperature experiment. **Figure** 2a shows the *I-V* curves measured from the TiN/L2NO4/Pt device in the standard RS mode measured at five different temperatures starting from RT (295 K) with increments of 30 K. It can be seen that when the device is switched to HRS, the current increases with the increase in temperature, which indicates the generation of additional charge carriers characteristic to semiconductors. A similar behavior, though not that apparent, is observed for LRS at negative polarity. However, in the LRS at positive polarity, the current decreases with the increase of the temperature, especially in the region of self-compliance. This "apparent metallicity" phenomenon was previously observed in $La_2NiO_{4+\delta}$ and is attributed to a carrier loss concomitant to the loss of oxygen occurring at increased temperatures.[68,69] Next, we analyzed the changes in SCLC behavior at elevated temperatures during the SET transition more closely. Figure 2b shows that at all temperatures, the *I–V* curves follow a similar behavior to the room temperature one (Figure S5a, Supporting Information). At the same time, interestingly, in the high voltage region, an increase in the trap-filled-limit voltage (V_{TFL}) is observed with the increase in temperature (inset in Figure 2b). Here, we determine the V_{TFL} as a voltage where the abrupt increase in the slope of the curve is observed, which is attributed to the transition from the shallow-trap SCLC to the trap-filled-limit SCLC.[67] This tendency can indicate an increase in the number of traps in the L2NO4 layer during the application of the negative bias.

While the analysis of the conduction mechanism can provide valuable information on carrier transport in the lattice, the experimental study of the oxygen migration in the film is essential for a deeper understanding of the resistive switching mechanism. Therefore, we implemented the XANES technique in operando mode, since it provides unique information about the electrochemical processes occurring in the memristive device. We specifically chose XANES for this investigation because it is an element-specific technique that is sensitive to small changes in the Ni oxidation state, so it can give insights into the oxygen migration in the L2NO4 layer, known for its ability to accommodate a large range of oxygen off-stoichiometry (δ).[30] First, the X-ray beam was focused on a selected pristine TiN/L2NO4/Pt device, with an initial resistance of 43.6 kΩ. The device was then operated in the standard RS mode. The XANES spectrum of the pristine state is shown in **Figure** 3a. The Ni–K edge position was defined as the inflection point (maximum of the first derivative) at 8345.5 eV (Figure 3d).

Next, the X-ray photon energy was set at the edge position and the Ni fluorescence intensity was continuously recorded while the device was electrically biased by bipolar voltage sweeps. This approach allows for faster measurements and puts in evidence the intensity changes corresponding to the Ni oxidization/reduction occurring under external electric polarization to

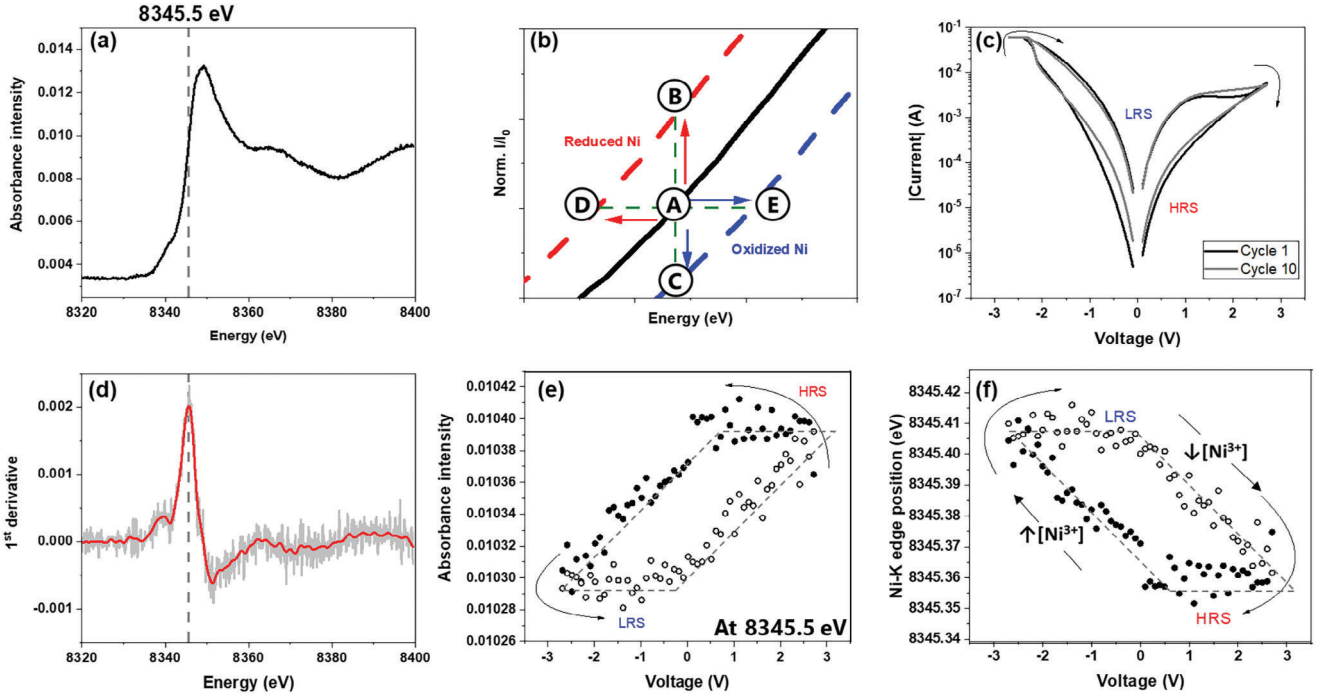

Figure 3. a) Ni–K edge XANES spectrum measured in the pristine state before operando XANES measurements to define the Ni–K edge position prior to any electrical bias. b) The schematics of the shifts from the pristine state and their interpretation in terms of oxidation or reduction of Ni. c) *I–V* characteristics in the standard RS mode for the 1st and 10th RS cycles were obtained from the TiN/L2NO4/Pt device during the operando XANES measurements. d) The first derivative plot is used for calculation of the Ni–K edge position. e) Absorbance intensity measured at 8345.5 eV averaged over ten RS cycles indicating changes in the Ni oxidation state with the voltage sweep application. f) Calculated Ni–K edge position averaged over 10 RS cycles. The dashed lines serve as a guide to the eye.

the device. Figure 3b shows the interpretation of the observed intensity changes by cycling for a shift of the Ni–K edge XANES spectrum. We observe that an intensity increase (from A to B) corresponds to a shift of the spectrum to lower energies (from A to D). Reversely, a decrease in the Ni–K edge intensity (from A to C) corresponds to a Ni–K edge shift to higher energies (from A to E when a negative voltage is applied to the device). Therefore, under voltage sweeps: 1) changes of Ni-fluorescence intensity were recorded (AB or AC); 2) shifts of Ni–K edge in energy were deduced (AD or AE); 3) Ni oxidation state changes were extracted. The combined *I–V* cycle and simultaneous X-ray absorption measurement at the edge position were carried out consecutively ten times (Figure S8, Supporting Information). The averaged intensity values for each applied voltage were then calculated (Figure 3e). The *I-V* characteristics of these sweeps are shown in Figure 3c. As described above, the Ni–K edge position can be deduced from the changes in the absorbance intensity and corresponding shifts of the Ni–K edge in energy (Figure 3f) using a rigid shift approach.

As observed in Figure 3f, when a negative voltage sweep is applied (SET process), Ni is oxidized (revealed by the increase in the Ni–K edge position or Ni oxidation state), corresponding to an oxygen concentration increase in L2NO4. It should be noted that the oxidation of L2NO4 occurs as soon as a small negative voltage is applied to the device, in a continuous manner from 0 to 2.7 V (maximum voltage applied). This could occur due to an oxygen ion drift from the TiN_xO_y layer into the L2NO4 film, as the oxygen ions are repelled by the negatively biased top TiN electrode. It can be observed that the rapid increase in current at 2.25 V is not accompanied by an abrupt change in oxidation state and could thus be related to the creation of a filament through the TiN_xO_y layer. Then, while the device is biased back from 2.7 to 0 V, the Ni oxidation state remains quite stable, indicating that the SET transition is complete with good retention of the LRS. At the forward sweep in opposite polarity (positive), the device gradually switches from LRS to HRS (RESET), while the Ni–K edge position progressively shifts back to lower energy, corresponding to the reduction of Ni (loss of oxygen in the L2NO4 film). In this case, oxygen ions from the L2NO4 would be re-incorporated into the TiN_xO_y layer, blocking the filament and re-creating a continuous insulating layer. Again, the Ni oxidation state change is gradual from 0 to +2.7 V (minimum voltage applied), while it then remains quite stable when sweeping back from +2.7 to 0 V, showing that the device's chemistry remains stable in HRS (horizontal dashed line in Figure 3e). This is consistent with the results of the resistance hysteresis switching loop (RHSL) test previously conducted for the TiN/L2NO4/Pt devices,[31] which showed that the resistance of the device remains stable at the back sweep in both polarities. These processes (resistance switching and Ni–K edge shift) are reversible, proving that L2NO4 acts as an oxygen exchange layer, and confirming that a valence change mechanism governs the standard RS mode in TiN/L2NO4/Pt devices. In addition, a similar tendency was observed when the device was operated in the interfacial RS mode (Figure S9, Supporting Information). The change of Ni–K edge between HRS and LRS is very small (≈0.07 eV), which corresponds to an average change in the

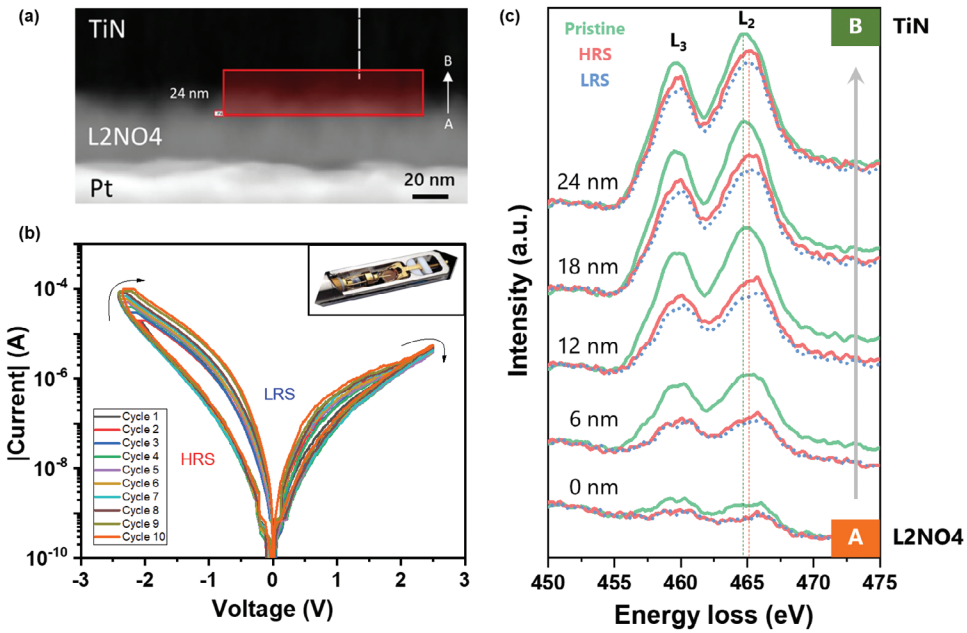

Figure 4. a) STEM image showing the geometry of the TiN/L2NO4/Pt TEM lamella device and the region of interest (ROI) marked by a red rectangle, which is 24 nm high and is centered at the TiN/L2NO4 interface. b) *I–V* curves taken from the lamella TiN/L2NO4/Pt device. Inset shows the sample holder used for the in situ electrical measurements. c) Comparison between Ti–$L_{2,3}$ edge EELS spectra obtained for the pristine state (green), HRS (red), and LRS (dashed blue) at five different positions of the selected ROI at the TiN/L2NO4 interface.

oxidation state of $\Delta x \approx 0.02$ and a change in oxygen content of $\Delta\delta \approx 0.01$. These very small changes show that the XANES operando methodology used here allows very subtle changes in oxidation state to be probed, providing evidence of the resistive switching mechanism taking place in these L2NO4-based memristive devices.

Next, the oxygen exchange between TiN and L2NO4 was investigated using in situ TEM. For this study, a region of interest (ROI) at the TiN/L2NO4 interface was selected (**Figure** 4a). It should be noted that the Ni–K edge EELS spectra overlap with the La $M_{4,5}$ edge, making the analysis overcomplicated, and thus these edges were not measured during the experiment. Therefore, the EELS spectra of the N–K edge, Ti–K edge, and O–K edge were acquired at the ROI for three different resistance states: pristine state, HRS, and LRS. First, STEM images (Figure S10, Supporting Information) and EELS spectra were taken in the pristine state prior to any electrical bias application (Figure S11, Supporting Information). Next, a series of voltage sweeps were applied to the TiN/L2NO4/Pt specimen with careful control of the current compliance, until RS was achieved (Figure 4b). At this moment, the lamella device was set to HRS and the EELS spectra were measured (Figure S12, Supporting Information). Next, the lamella device was set to LRS with the 0 V → −2.5 V → 0 V voltage sweep, and EELS spectra were taken for the LRS state (Figure S13, Supporting Information). It should be noted that although the *I–V* curves measured from the lamella device are similar in shape, they do not reach the same exact current densities as those measured for standard 50 μm^2 devices (Figure S14, Supporting Information).

In general, the EELS spectra show that the N–K edge intensity is highest at point B (top, 24 nm, see Figure 4a), gradually decreases, and mostly disappears at point A (bottom, 0 nm), confirming that, as expected, nitrogen is present within the TiN top electrode. Similar observations are obtained for titanium: the Ti-$L_{2,3}$ edge intensity is highest at point B, then slowly decreases, and is barely visible at point A, for the pristine state, HRS, and LRS. Although the oxygen spectra are relatively noisy (compared to the Ti spectra) in the three resistance states, it can be observed that the O–K edge becomes visible and broader along the B → A direction (from the TiN layer to the L2NO4 film), confirming the presence of oxygen in the L2NO4 film. As its intensity is very low even within the L2NO4 film, its presence within the interlayer is difficult to evaluate.

Since the clearest changes between different positions and states are observed for the Ti-$L_{2,3}$ edge spectra, we have chosen to focus on these spectra and compare them in more detail. An energy shift in the EELS spectrum or changes in the fine structure can indicate a change in crystallographic structure or chemical composition.[70] L_2 and L_3 edges are mainly studied as the main features to analyze EELS spectra of transition metals (such as Ti). Indeed, due to spin-orbit splitting of the 2p core hole, when an electron is excited, its transition from the 2p to the 3d states is known as the Ti-L_3 edge ($2p_{3/2}$ → 3d) and Ti-L_2 edge ($2p_{1/2}$ → 3d).[71] Abdallah et al. studied the chemical shift of the EELS Ti-$L_{2,3}$ edges to determine the composition at different regions of a sample through an oxide-alloy interface consisting of oxide, titanium oxynitride interface, titanium nitride and Ti-based alloy ($Ti_6Al_2Sn_4Zr_2Mo_{0.1}Si$).[70] In this study, the Ti–L_3 and the Ti–L_2 edges in the alloy were found at 457.0 and 462.5 eV, respectively. The spectra are shifted to higher energies when entering the TiN region, then to even higher energies with broader peaks in the titanium oxynitride interface and, finally, start splitting into four peaks ($t_{2g} + e_{2g}$ for each L_3 and L_2) when reaching the oxide

region. Indeed, depending on the Ti valence and the atomic surrounding degeneracy of Ti^{4+} can occur, leading to the splitting of unoccupied 3d into lower t_{2g} and higher e_g bands.[72] Based on these features, we analyzed the oxidation of Ti (presence of Ti^{4+}) in this work.

For a careful comparison of the oxidation state changes, the EELS spectra at the Ti–$L_{2,3}$ edges for the pristine state, HRS, and LRS are plotted in Figure 4c. Only the representative spectra at 0 (point A), 6, 12, 18, and 24 nm (point B) within the ROI are shown (marked with a rectangle in Figure 4a). In the pristine state (green spectra) at the top part of the ROI (positions: 24, 18, and 12 nm), the Ti–L_2 and Ti–L_3 edges are detected at 459.6 and 464.8 eV, respectively, which are shifted to higher energies compared to those reported for the TiN in the literature (≈458.6 eV and ≈463.6 eV).[73] However, as stated in the experimental section, the TiN used in this study is thought to be slightly off-stoichiometric, therefore, we can conclude that the top part of ROI is mainly TiN_x. At the bottom part of the ROI, the Ti–$L_{2,3}$ edges are broader and are shifted to higher energies, suggesting a TiN_xO_y interlayer is present. In HRS (red spectra), the Ti–$L_{2,3}$ edges at all ROIs are shifted to higher energies, compared to those in the pristine state (green spectra). In addition, the spectra for the bottom positions (0 to 12 nm) become more asymmetric with a higher intensity at higher energy (≈ 465.8 eV). This observation suggests that the TiN_xO_y interface is further oxidized due to the drift of oxygen from L2NO4 to TiN (triggered by the positive voltage sweep). Due to the good control of the in situ experiments, it was possible to apply many voltage sweeps on the thin TEM lamella during the transformation from the pristine state to the HRS. In LRS (dashed blue spectra), the aforementioned peaks seem to slightly decrease in intensity, and seem to be slightly flatter and less asymmetric compared to HRS (red spectra), suggesting that the ratio of Ti^{4+}/Ti^{3+} decreases. These small changes can be explained by the reduction of the TiN_xO_y, which is related to oxygen ions drifting back into the L2NO4 film under negative bias. It should be noted that the observed changes in the EELS spectra between HRS and LRS are very small, so from these data alone it would not be possible to confirm the redox reaction at the TiN/L2NO4 interface. However, as previously mentioned, using operando XANES measurements, a variation in oxygen content in the L2NO4 film of $\Delta\delta \approx 0.01$ during cycling was observed, which is difficult to measure by other methods. In addition, the Ti–$L_{2,3}$ edge EELS spectra of the pristine state (green) and those of the LRS (blue) are very different, suggesting that the structure and chemical composition of the ROI has changed upon repetitive cycling, and the device does not come back to the same structural and chemical characteristics of the pristine state.

Based on the combination of the operando XANES, the in situ TEM observations, the electrical characteristics, and the study of the conduction mechanism of the TiN/L2NO4/Pt device presented in this work, we propose a complete model for both RS modes presented in **Figure 5**. First, during the deposition of titanium nitride, a TiN_xO_y interlayer is naturally formed at the TiN/L2NO4 interface by the intake of oxygen. This fact was previously shown by EDX measurements[31] and was confirmed by the in situ TEM/EELS observations in this work (Figure 4c). Under the first application of positive voltage, oxygen ions drift from L2NO4 toward TiN, further oxidizing the TiN_xO_y interlayer, and leading to a slight increase in the resistance of the device, as observed on the positive polarity of the *I–V* curve in Figure 1a. In addition, the loss of oxygen ions (decrease in δ) makes L2NO4 more resistive due to the decrease in the number of hole carriers.[30] Therefore, the increase of the series resistance of the device occurs due to the decrease in the oxygen vacancy concentration in the TiN_xO_y layer and the decrease in oxygen ion concentration in the L2NO4 layer. In the opposite polarity, when a negative voltage is applied to TiN, an electrochemical redox reaction takes place to reduce the TiN_xO_y, and oxygen ions are reincorporated into L2NO4, which gets oxidized. The capability of oxygen transport between the L2NO4 and TiN_xO_y layers before the "soft-forming" process is also confirmed by Ni–K edge position shifts observed during operando XANES measurements for the interfacial RS mode (Figure S9, Supporting Information). Therefore, we believe that an interfacial process underlies the small difference between the resistance states observed in Figure 1a at the $|V_{max}| \leq 2$ V, which is also evident from the area dependence of HRS and LRS resistance (Figure S1a, Supporting Information). The schematics of the oxygen exchange under external bias in the interfacial RS mode are shown in Figure 5a.

Furthermore, for the standard RS mode, we propose a coexistence of a filament-based and an interface-based valence change switching mechanism. At a certain negative voltage V_F, the oxygen vacancy concentration within the TiN_xO_y interlayer would become large enough to create conducting paths (CF in the form of TiN_x) and the LRS of the standard RS mode would be reached (Figure 5b). Therefore, from the second cycle on, the standard RS mode is believed to be related to the formation/annihilation of the CF(s) of TiN_x in TiN_xO_y. Indeed, as seen in Figure S1b (Supporting Information), after the soft electroforming the HRS and LRS do not scale with electrode area, which is a typical characteristic of filamentary RS. This type of switching is also supported by the abrupt decrease in resistance (switch from HRS to LRS), which is not accompanied by a large change in the Ni oxidation state in operando XANES (Figure 3f), suggesting the filament formation/rupture occurs in the TiN_xO_y layer and not in the L2NO4 layer. It is important to acknowledge that in actual devices, the TiN/L2NO4 interface does not exhibit perfect flatness, as depicted in the model for simplicity. Additionally, the thickness of the interlayer is not entirely uniform due to the roughness of the L2NO4 film,[31] as evidenced by STEM observations (see Figure 4a). In the regions where the TiN_xO_y interlayer is thinner, the localized electric field enhancement could lead to a local CF formation in the area under negative bias.[74–76] In turn, the L2NO4 film in standard RS mode would act as an oxygen reservoir layer, where the oxygen entering or coming out from the L2NO4 can be indirectly measured by the change in Ni oxidation state in the operando Ni–K edge XANES measurements. Figure 5c shows the proposed switching mechanism for the standard RS mode. Under positive bias, oxygen drift from L2NO4 into TiN would take place, first reducing the oxygen ion concentration within the L2NO4 (and thus more resistive L2NO4 is obtained), second further oxidizing the TiN_xO_y interlayer, and ultimately disconnecting the conductive filaments of TiN_x (reaching an HRS). Reversibly, the LRS is reached when the filaments are re-connected, favored by the reduction of TiN_xO_y and the drift of oxygen ions back into the L2NO4 film, decreasing its resistivity

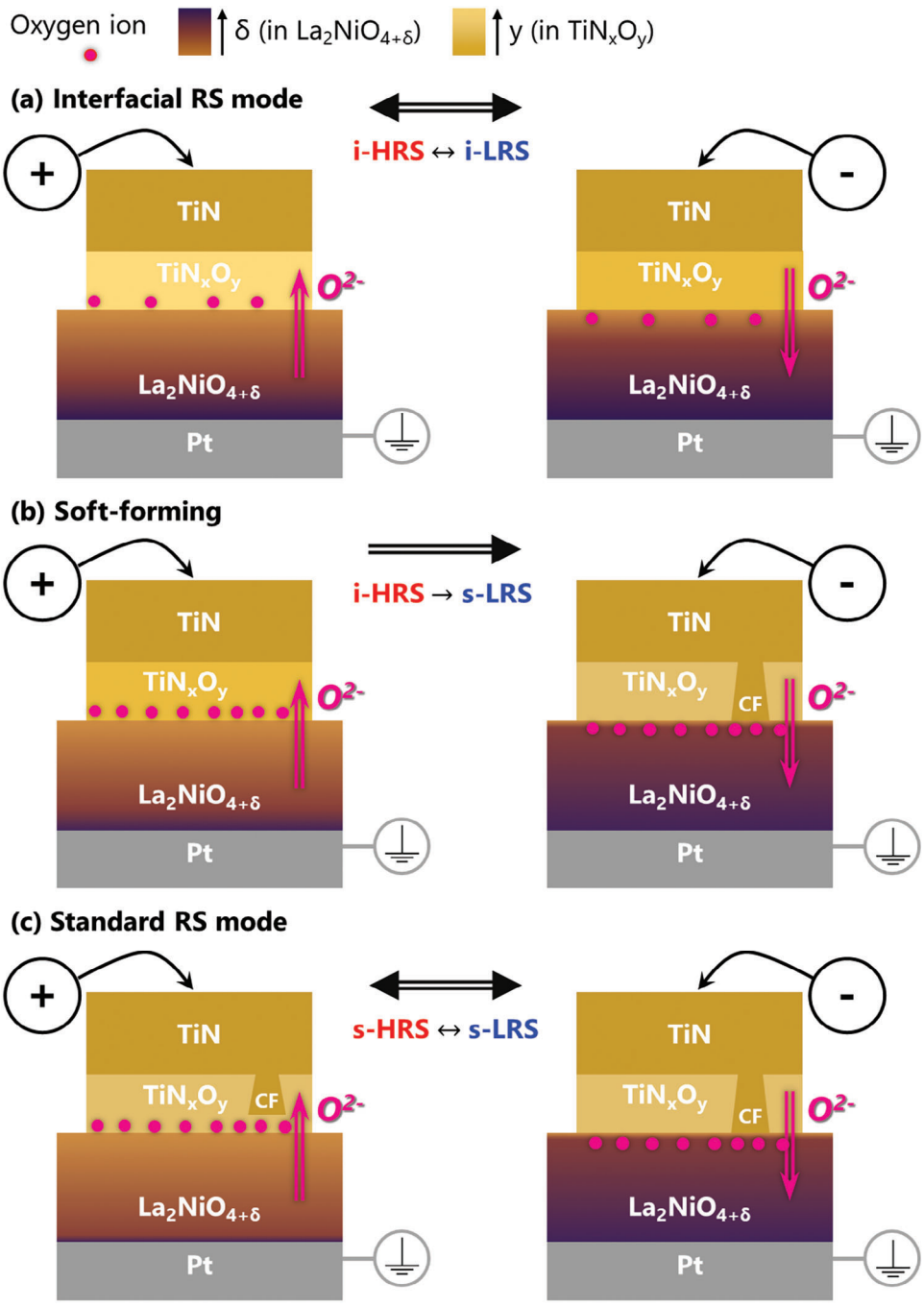

Figure 5. Phenomenological model of the resistive switching mechanism in TiN/L2NO4/Pt vertical devices. To picture the oxygen concentration differences in L2NO4 and TiN/TiN_xO_y layers, we used color gradients. In addition, we added the pink circles to emphasize the oxygen ions migration between the L2NO4 and TiN_xO_y layers and their role in the formation/disruption of the conductive filament in the TiN_xO_y layer. a) During the TiN deposition, oxygen scavenging takes place and the TiN_xO_y layer is formed at the TiN/L2NO4 interface. Under the application of bias below V_F, a small amount of oxygen ions migrates between the TiN_xO_y and the L2NO4 layers, resulting in interfacial switching with a small HRS/LRS ratio. b) With the application of an increased negative bias (V_F), oxygen migration from TiN_xO_y to L2NO4 intensifies, leading to the creation of a CF in the TiN_xO_y layer in the form of TiN_x. c) Standard RS mode: at positive polarity, the RESET process occurs due to the oxygen migration from L2NO4 to TiN_xO_y, leading to the rupture of the CF in the TiN_xO_y layer and a decrease in hole carrier concentration in the L2NO4 layer. At negative polarity, the SET process occurs due to the oxygen migration from TiN_xO_y to L2NO4, leading to the formation of a CF in the TiN_xO_y layer and an increase in the hole carrier concentration in the L2NO4 layer.

by generating additional hole carriers in the bulk. The reconnection of the filaments coincides with the complete filling of the traps with carriers observed in Figure 2b when the trap sites no longer affect the current conduction because they are neutralized by the trapped carriers. According to the drift-diffusion model developed for SCLC in MIECs,[77] the migration of negative ions away from the negatively biased electrode creates an excess negative electric field at the interface of this electrode with the MIEC, which can induce oxygen migration toward the L2NO4 layer and facilitate the CF formation. Finally, we believe that the behavior of *I–V* curves as a function of the temperature (Figure 2) is in good agreement with our spectroscopic results. The mobility of interstitial oxygen ions in the L2NO4 layer increases with temperature, which means that more oxygen can move from the TiN_xO_y interlayer to the bulk of the L2NO4 under negative bias. Consecutively, since the oxygen ions act as traps for holes during carrier transport through the film, an increase in the trap concentration leads to the observed V_{TFL} increase. On the other hand, at positive polarity, due to the increased mobility at the elevated temperatures oxygen ions drift quickly toward the positively biased TiN electrode. In turn, as was mentioned in the description to Figure 2, in L2NO4 the loss of oxygen is followed by a reduction in the hole carriers concentration.[68,78] Therefore, the migration of oxygen to the TiN_xO_y layer leads to the simultaneous decrease in the hole carrier concentration, resulting in the self-compliance effect observed, which becomes more pronounced at higher temperatures.

3. Conclusion

In this work, the resistive switching mechanism of TiN/L2NO4/Pt devices was studied by spectroscopic methods in addition to electrical measurements as a function of temperature and conduction mechanism analysis. To get a deep insight into the RS process, an original operando XANES methodology was developed. This approach involves continuous monitoring of the Ni–K edge at a fixed photon energy, with the X-ray beam focused on a single device throughout its cycling, making it possible to follow the oxygen exchange between the TiN_xO_y interlayer and the L2NO4 film in real time. in situ TEM/EELS observations on a TiN/L2NO4/Pt specimen (lamella device) proved to be a unique complementary technique, revealing the oxidation/reduction dynamics of TiN_xO_y during the switching process. The combined electrical and spectroscopic characterization results strongly suggest that the TiN/L2NO4/Pt devices exhibit two different switching modes: interfacial RS mode and standard RS mode (filamentary + interfacial). Before the "soft forming" event, interface-type RS is dominant due to the oxygen drift under the external electric field. After being formed, the standard RS mode in TiN/L2NO4/Pt devices would be controlled by the formation/dissolution of TiN_x CF(s) in the TiN_xO_y interlayer governed by the oxygen exchange with the L2NO4 reservoir layer and by the change in L2NO4 layer oxygen stoichiometry. We believe that our findings and novel operando XANES approach can be extended to many other systems allowing for a better understanding of the mechanisms underlying the behavior of valence change memories.

Table 1. . Parameters used for the deposition of L2NO4 thin films by PI-MOCVD.

Parameters	Value
Injection frequency	1 Hz
Opening time	2 ms
Number of pulses	2000
Evaporation temperature	220–280 °C
Substrate temperature	600 °C
Carrier gas	218 sccm (34% Ar) + 418 sccm (66% O_2)
Total pressure inside the reactor	5 Torr

4. Experimental Section

Thin Film Fabrication: Polycrystalline $La_2NiO_{4+\delta}$ films were deposited on 1 × 1cm^2 substrates which consist of Pt (100 nm)/TiO_2 (20 nm)/SiO_2 (500 nm)/Si (750 µm)/SiO_2 (500 nm) structures from top to bottom, supplied by CEA-Leti. The L2NO4 thin films were synthesized by pulsed injection metal–organic chemical vapor deposition (PI-MOCVD).[28,31] La(tmhd)3 (tris(2,2,6,6-tetramethyl-3,5-heptanedionato)lanthanum(III)) and [Ni(tmhd)2] (bis(2,2,6,6-tetramethyl-3,5-heptanedionato)nickel(II)) precursors from Strem Chemicals were dissolved in a 0.02 M solution with m-xylene (1,3-dimethylbenzene) from Alfa Aesar. The L2NO4 growth conditions used in this work are detailed in **Table 1** and correspond to the optimized deposition conditions for L2NO4 thin films grown on Pt.[28] The ellipsometry measurements were performed on the L2NO4/Pt structures using a Semilab SE-2000 spectral ellipsometer at the 75° angle to study the optical properties and assess the refractive index of the L2NO4 film. The spectra were fitted using the combination of the Cauchy and Lorentz models in the OEA software in the photon energy range of 1.53–6.44 eV. The thickness of the L2NO4 layer (≈33 nm) was estimated using cross-section TEM measurements.

Device Fabrication: The microfabrication of the devices was carried out in the PTA clean-room facilities (Grenoble), including laser lithography (Heidelberg instrument µPG 101) and deposition of ≈100 nm thick TiN top electrode by reactive sputtering equipment (PVD 100 Alliance Concept, the deposition rate is 0.2 nm s^1). It should be noted that although for simplicity the stoichiometry TiN formula is used, the exact stoichiometry of the sputtered TiN has not been measured. However, it is thought to be slightly off-stoichiometric (e.g., $TiN_{x<1}$), as its nominal resistivity of 88 µΩ cm is higher than the theoretical value of 20 µΩ.cm expected for stoichiometric TiN. It should also be noted that fully stoichiometric TiN is a metal with a relatively high work function and a relatively low oxygen affinity[79] often used in the industry,[54] similar to Pt, Ir, or Au. On the other hand, $TiN_{x<1}$ is often obtained in research laboratories as a non-stoichiometric nitride which can act as an oxidizable electrode, such as Ti, Ta, W, and Hf, due to the excess of Ti in the structure.

Electrical Characterization: The current-voltage measurements were carried out on TiN/L2NO4/Pt devices using a Keithley 4200 semiconductor parameter analyzer in sweep mode using a source measurement unit and two external micromanipulators. The voltage was applied at the top TiN electrode while the bottom Pt electrode was grounded. In sweep mode, the bipolar triangular voltage sweeps always follow the sequence: 0 V → $+V_{max}$ → 0 V → $-V_{max}$ → 0 V, with voltage steps of 0.01 V. After each half cycle (0 V → $+V_{max}$ → 0 V or 0 V → $-V_{max}$ → 0 V), a sweep (0 V → 0.01 V) was applied to readout the resistance. The current compliance was limited to 100 mA at the negative branch to prevent device breakdown. All the measurements in this work were carried out on square devices with a top electrode area of 50×50 µm^2 (if not otherwise specified).

Operando XANES: The operando XANES measurements were carried out at the ID12 beamline[80] of the ESRF Synchrotron (Grenoble, France). The picture of the experimental setup is shown in Figure S6 (Supporting Information). The photon source is the APPLE-II type helical undulator HU-38 at the fundamental harmonic of its emission. A Ni foil and a NiO

powder were measured as references for the Ni (0) and Ni (II) oxidation states. These XANES measurements of these references were corrected for the self-absorption effect. The energy position of the first inflection point (maximum of the first derivative) in the Ni K-edge XANES spectra was used as the energy of the edge for all measurements. The Ni foil edge position was calibrated against the known K-edge position of Ni(0), 8333.0 eV, and the same offset was applied to all XANES measurements. The Ni–K edge values measured for the NiO powder, corresponding to Ni (II), are close to the calibration curve established by Woolley et al.[81] Thus, the same calibration curve was used in this work to estimate the Ni oxidation state (Figure S7, Supporting Information), from which the oxygen off-stoichiometry (δ) was derived by charge balance.

For the TiN/L2NO4/Pt samples with memristive devices, XANES spectra were acquired for selected regions (focusing the beam using Be refractive lenses) at room temperature. The spectra were recorded in fluorescence yield detection mode using two silicon drift diode detectors in a backscattering configuration. To minimize elastic scattering, a 10 µm Co foil was inserted in front of the detectors. For accurate XANES mapping, a beam size smaller than the electrode area was used (the precise beam size is detailed in each case). Typically, two to four scans were carried out and averaged to improve the statistics. To apply the external electrical bias during operando measurements, a Keithley 2410 source meter was employed. In this case, the voltage was applied to the Pt electrode while the TiN electrode was grounded. Nevertheless, for simplicity and consistency throughout the article, all the *I-V* curves are plotted using the Pt electrode as the virtual ground.

In Situ TEM: For in situ TEM experiments, a 120 nm thick lamella was prepared by focused ion beam (FIB) milling in an FEI Strata 400S. The lamella was then mounted in a Hummingbird sample holder, which has a piezo-controlled motor, allowing for the movement of an electrical probe that can be used to provide electrical contact. The Pt bottom electrode was grounded to a standard copper grid and a tungsten tip was landed on the top of the TiN electrode. It should be noted that the electrical contact is far away from the regions where the TEM observations were carried out. Just before the experiments, the sample was exposed to an oxygen-argon plasma cleaning. The TEM observations of the samples were performed in an ultra-high vacuum using a double-aberration-corrected FEI Titan Ultimate TEM equipped with a high-brightness electron source and a Gatan Tridiem energy filter equipped with Dual EELS. A beam current of 200 pA was used. The specimen was electrically biased using a Keithley 2600 source meter. A 24 nm wide region of interest was selected at the TiN/L2NO4 interface, where EELS spectra were measured and then integrated for three resistance states (pristine, HRS, and LRS).

Supporting Information

Supporting Information is available from the Wiley Online Library or from the author.

Acknowledgements

T.-K.K. and A.K. contributed equally to this work and share the first authorship. This work was partially supported by the LabEx Minos ANR-10-LABX-55-01 (for T.-K.K.), by ANR France within the "Mangaswitch" Project ANR-17-CE24-0038 and has also received financial support from the CNRS through the MITI interdisciplinary programs ("Synconnect" 80|PRIME project). This research has benefited from characterization equipment of the Grenoble INP–CMTC platform supported by the Centre of Excellence of Multifunctional Architectured Materials "CEMAM" n°ANR-10-LABX-44-01 funded by the "Investments for the Future" Program. Part of this work, carried out on the Platform for Nanocharacterization (PFNC), was supported by the "Recherches Technologiques de Base" program of the French National Research Agency (ANR). In addition, the work was performed with the help of the "Plateforme Technologique Amont (PTA)" in Grenoble, with the financial support of the "Nanosciences aux limites de la Nanoélectronique" Foundation and CNRS Renatech network. The authors acknowledge Valentine Bolcato (PTA, Grenoble INP, France) for the deposition of the TiN layer. The authors acknowledge the European Synchrotron Radiation Facility (ESRF) for the provision of synchrotron radiation facilities and would like to thank Fabrice Wilhelm for assistance and support in using beamline ID12.

Conflict of Interest

The authors declare no conflict of interest.

Data Availability Statement

The data that support the findings of this study are available from the corresponding author upon reasonable request.

Keywords

in-situ TEM, $La_2NiO_{4+\delta}$, operando XANES, resistive switching mechanism, valence change memory

Received: April 19, 2024
Revised: June 6, 2024
Published online:

[1] K. Sun, J. Chen, X. Yan, *Adv. Funct. Mater.* **2021**, *31*, 2006773.
[2] H. Li, S. Wang, X. Zhang, W. Wang, R. Yang, Z. Sun, W. Feng, P. Lin, Z. Wang, L. Sun, Y. Yao, *Adv. Int. Syst.* **2021**, *3*, 2100017.
[3] D. Ielmini, Z. Wang, Y. Liu, *APL Mater* **2021**, *9*, 050702.
[4] G. Pedretti, D. Ielmini, *Electronics (Basel)* **2021**, *10*, 1063.
[5] D. Ielmini, S. Ambrogio, *Nanotechnology* **2020**, *31*, 092001.
[6] P. Mannocci, M. Farronato, N. Lepri, L. Cattaneo, A. Glukhov, Z. Sun, D. Ielmini, *APL Machine Learning* **2023**, *1*, 010902.
[7] D. Ielmini, *Semicond. Sci. Technol.* **2016**, *31*, 063002.
[8] I. H. Inoue, A. Sawa, in *Functional Metal Oxides*, Vol. *11*, Wiley-VCH Verlag GmbH & Co. KGaA, Weinheim, Germany **2013**, pp. 443–463.
[9] D. Panda, T.-Y. Tseng, *Ferroelectrics* **2014**, *471*, 23.
[10] S. Bagdzevicius, K. Maas, M. Boudard, M. Burriel, *J Electroceram* **2017**, *39*, 157.
[11] A. A. Minnekhanov, A. V. Emelyanov, D. A. Lapkin, K. E. Nikiruy, B. S. Shvetsov, A. A. Nesmelov, V. V. Rylkov, V. A. Demin, V. V. Erokhin, *Sci. Rep.* **2019**, *9*, 10800.
[12] A. N. Matsukatova, A. V. Emelyanov, A. A. Minnekhanov, A. A. Nesmelov, A. Y. Vdovichenko, S. N. Chvalun, V. V. Rylkov, P. A. Forsh, V. A. Demin, P. K. Kashkarov, M. V. Kovalchuk, *Appl. Phys. Lett.* **2020**, *117*, 243501.
[13] H. L. Park, M. H. Kim, M. H. Kim, S. H. Lee, *Nanoscale* **2020**, *12*, 22502.
[14] J. L. Rieck, F. V. E. Hensling, R. Dittmann, *APL Mater* **2021**, *9*, 021110.
[15] F. V. E. Hensling, H. Du, N. Raab, C. L. Jia, J. Mayer, R. Dittmann, *APL Mater.* **2019**, *7*, 101127.
[16] T. Heisig, J. Kler, H. Du, C. Baeumer, F. Hensling, M. Glöß, M. Moors, A. Locatelli, T. O. Menteş, F. Genuzio, J. Mayer, R. A. De Souza, R. Dittmann, *Adv. Funct. Mater.* **2020**, *30*, 2004118.
[17] C. Funck, C. Bäumer, S. Wiefels, T. Hennen, R. Waser, S. Hoffmann-Eifert, R. Dittmann, S. Menzel, *Phys. Rev. B* **2020**, *102*, 035307.
[18] R. Muenstermann, T. Menke, R. Dittmann, R. Waser, *Adv. Mater.* **2010**, *22*, 4819.
[19] R. Rodriguez-Lamas, D. Pla, C. Pirovano, O. Chaix-Pluchery, C. Moncasi, M. Boudard, R.-N. Vannier, C. Jiménez, M. Burriel, *Mater. Today Electr.* **2023**, *5*, 100054.

[20] B. Meunier, E. Martinez, R. Rodriguez-Lamas, D. Pla, M. Burriel, C. Jimenez, Y. Yamashita, O. Renault, *ACS Appl. Electr. Mater.* **2021**, *3*, 5555.
[21] B. Meunier, E. Martinez, R. Rodriguez-Lamas, D. Pla, M. Burriel, M. Boudard, C. Jiménez, J.-P. Rueff, O. Renault, *J. Appl. Phys.* **2019**, *126*, 225302.
[22] C. Moncasi, G. Lefèvre, Q. Villeger, L. Rapenne, H. Roussel, A. Bsiesy, C. Jiménez, M. Burriel, *Adv. Mater. Interfaces* **2022**, *9*, 2200498.
[23] C. Moncasi, G. Lefèvre, Q. Villeger, L. Rapenne, T. Khuu, F. Wilhelm, A. Rogalev, C. Jiménez, M. Burriel, *Adv. Mater. Interfaces* **2023**, *10*, 2202496.
[24] K. Moon, E. Cha, J. Park, S. Gi, M. Chu, K. Baek, B. Lee, S. H. Oh, H. Hwang, *IEEE Electron Device Lett.* **2016**, *37*, 1067.
[25] D. Lee, K. Moon, J. Park, S. Park, H. Hwang, *Appl. Phys. Lett.* **2015**, *106*, 113701.
[26] S. Park, M. Siddik, J. Noh, D. Lee, K. Moon, J. Woo, B. H. Lee, H. Hwang, *Semicond. Sci. Technol.* **2014**, *29*, 104006.
[27] S. Park, A. Sheri, J. Kim, J. Noh, J. Jang, M. Jeon, B. Lee, B. R. Lee, B. H. Lee, H. Hwang, In *2013 IEEE Int. Electron Devices Meeting*, IEEE, Washington, DC, USA **2013**, pp. 25.6.1-25.6.4.
[28] T. Khuu, G. Lefèvre, C. Jiménez, H. Roussel, A. Riaz, S. Blonkowski, E. Jalaguier, A. Bsiesy, M. Burriel, *Adv. Mater. Technol.* **2022**, *7*, 2200329.
[29] K. Maas, E. Villepreux, D. Cooper, C. Jiménez, H. Roussel, L. Rapenne, X. Mescot, Q. Rafhay, M. Boudard, M. Burriel, *J. Mater. Chem. C. Mater.* **2020**, *8*, 464.
[30] K. Maas, E. Villepreux, D. Cooper, E. Salas-Colera, J. Rubio-Zuazo, G. R. Castro, O. Renault, C. Jimenez, H. Roussel, X. Mescot, Q. Rafhay, M. Boudard, M. Burriel, *Adv. Funct. Mater.* **2020**, *30*, 1909942.
[31] T.-K. Khuu, A. Koroleva, A. Degreze, E.-I. Vatajelu, G. Lefèvre, C. Jiménez, S. Blonkowski, E. Jalaguier, A. Bsiesy, M. Burriel, *J. Phys. D. Appl. Phys.* **2024**, *57*, 10LT01.
[32] S. Menzel, R. Waser, in *Advances in Non-volatile Memory and Storage Technology*, 2nd ed., Elsevier, Amsterdam **2019**, p. 137.
[33] A. Wedig, M. Luebben, D.-Y. Cho, M. Moors, K. Skaja, V. Rana, T. Hasegawa, K. K. Adepalli, B. Yildiz, R. Waser, I. Valov, *Nat. Nanotechnol.* **2016**, *11*, 67.
[34] C.-F. Chang, J.-Y. Chen, C.-W. Huang, C.-H. Chiu, T.-Y. Lin, P.-H. Yeh, W.-W. Wu, *Small* **2017**, *13*, 1603116.
[35] B. Hajri, H. Aziza, M. M. Mansour, A. Chehab, *IEEE Access* **2019**, *7*, 168963.
[36] K. Kamiya, M. Y. Yang, B. Magyari-Köpe, Y. Nishi, K. Shiraishi, in *Advances in Non-volatile Memory and Storage Technology*, Elsevier, Amsterdam **2014**, p. 262.
[37] S. Ambrogio, B. Magyari-Köpe, N. Onofrio, M. Mahbubul Islam, D. Duncan, Y. Nishi, A. Strachan, *J. Electroceram* **2017**, *39*, 39.
[38] B. Traore, P. Blaise, B. Sklenard, E. Vianello, B. Magyari-Kope, Y. Nishi, *IEEE Trans. Electron Devices* **2018**, *65*, 507.
[39] R. Chaurasiya, P. E. Lin, C. H. Lyu, K. T. Chen, L. C. Shih, J. S. Chen, *Nanotechnology* **2022**, 33.
[40] W. Sun, B. Gao, M. Chi, Q. Xia, J. J. Yang, H. Qian, H. Wu, *Understanding Memristive Switching via In Situ Characterization and Device Modeling*, Vol. *10*, Nature Publishing Group, Berlin, Germany **2019**.
[41] Y. Zhang, C. Wang, X. Wu, *Nanoscale* **2022**, *14*, 9542.
[42] C. N. Peng, C. W. Wang, T. C. Chan, W. Y. Chang, Y. C. Wang, H. W. Tsai, W. W. Wu, L. J. Chen, Y. L. Chueh, *Nanoscale Res. Lett.* **2012**, *7*, 1.
[43] Y. Yang, P. Gao, S. Gaba, T. Chang, X. Pan, W. Lu, *Nat. Commun.* **2012**, *3*, 732.
[44] H. Jiang, L. Han, P. Lin, Z. Wang, M. H. Jang, Q. Wu, M. Barnell, J. J. Yang, H. L. Xin, Q. Xia, *Sci. Rep.* **2016**, *6*, 28525.
[45] D.-H. Kwon, K. M. Kim, J. H. Jang, J. M. Jeon, M. H. Lee, G. H. Kim, X.-S. Li, G.-S. Park, B. Lee, S. Han, M. Kim, C. S. Hwang, *Nat. Nanotechnol.* **2010**, *5*, 148.
[46] J. Kwon, Y. N. Picard, M. Skowronski, A. A. Sharma, J. A. Bain, In 2014 IEEE International Reliability Physics Symposium, IEEE, Piscataway, NJ **2014**, pp. 5E.5.1-5E.5.5.
[47] K. Baek, S. Park, J. Park, Y.-M. Kim, H. Hwang, S. H. Oh, *Nanoscale* **2017**, *9*, 582.
[48] A. Ranjan, H. Xu, C. Wang, J. Molina, X. Wu, H. Zhang, L. Sun, J. Chu, K. L. Pey, *Appl. Mater. Today* **2023**, *31*, 101739.
[49] D. Cooper, C. Baeumer, N. Bernier, A. Marchewka, C. La Torre, R. E. Dunin-Borkowski, S. Menzel, R. Waser, R. Dittmann, *Adv. Mater.* **2017**, *29*, 1700212.
[50] Y. Shih, L. Lee, K. Liang, A. Manikandan, W. Liu, Y. Chen, M. Chang, Z. M. Wang, Y. Chueh, *Adv. Electron. Mater.* **2021**, *7*, 2000252.
[51] C. Lenser, A. Kuzmin, J. Purans, A. Kalinko, R. Waser, R. Dittmann, *J. Appl. Phys.* **2012**, *111*, 076101.
[52] M. Janousch, G. I. Meijer, U. Staub, B. Delley, S. F. Karg, B. P. Andreasson, *Adv. Mater.* **2007**, *19*, 2232.
[53] L. J. A. Macedo, A. Hassan, G. C. Sedenho, F. N. Crespilho, *Nat. Commun.* **2020**, *11*, 316.
[54] R. Dittmann, S. Menzel, R. Waser, *Adv. Phys.* **2021**, *70*, 155.
[55] A. A. Koroleva, M. G. Kozodaev, Y. Y. Lebedinskii, A. M. Markeev, *J Phys D Appl Phys* **2021**, *54*, 504004.
[56] A. A. Koroleva, D. S. Kuzmichev, M. G. Kozodaev, I. V. Zabrosaev, E. V. Korostylev, A. M. Markeev, *Appl. Phys. Lett.* **2023**, *122*, 022905.
[57] C. Mahata, M. Kang, S. Kim, *Nanomaterials* **2020**, *10*, 2069.
[58] J. Kang, T. Kim, S. Hu, J. Kim, J. Y. Kwak, J. Park, J. K. Park, I. Kim, S. Lee, S. Kim, Y. Jeong, *Nat. Commun.* **2022**, *13*, 4040.
[59] L. Zhao, H.-Y. Chen, S.-C. Wu, Z. Jiang, S. Yu, T.-H. Hou, H.-S. P. Wong, Y. Nishi, *Nanoscale* **2014**, *6*, 5698.
[60] T. Tan, Y. Du, A. Cao, Y. Sun, G. Zha, H. Lei, X. Zheng, *J. Alloys Compd.* **2018**, *766*, 918.
[61] E. Lim, R. Ismail, *Electronics (Basel)* **2015**, *4*, 586.
[62] F. Chen, S.-W. Wang, L. Yu, X. Chen, W. Lu, *Opt. Mater. Express* **2014**, *4*, 1833.
[63] M. Burriel, G. Garcia, M. D. Rossell, A. Figueras, G. Van Tendeloo, J. Santiso, *Chem. Mater.* **2007**, *19*, 4056.
[64] A. Rose, *Phys. Rev.* **1955**, *97*, 1538.
[65] M. A. Lampert, *Phys. Rev.* **1956**, *103*, 1648.
[66] J. Bai, W. Xie, W. Zhang, Z. Yin, S. Wei, D. Qu, Y. Li, F. Qin, D. Zhou, D. Wang, *Appl. Surf. Sci.* **2022**, *600*, 154084.
[67] P. Zhang, Y. S. Ang, A. L. Garner, Á. Valfells, J. W. Luginsland, L. K. Ang, *J. Appl. Phys.* **2021**, *129*, 100902.
[68] J. M. Bassat, P. Odier, J. P. Loup, *J. Solid State Chem.* **1994**, *110*, 124.
[69] S. Nishiyama, D. Sakaguchi, T. Hattori, *Solid State Commun.* **1995**, *94*, 279.
[70] I. Abdallah, C. Dupressoire, L. Laffont, D. Monceau, A. Vande Put, *Corros. Sci.* **2019**, *153*, 191.
[71] R. D. Leapman, L. A. Grunes, P. L. Fejes, *Phys. Rev. B* **1982**, *26*, 614.
[72] D. W. Fischer, *J. Appl. Phys.* **1970**, *41*, 3561.
[73] S. Terada, K. Asayama, M. Tsujimoto, H. Kurata, S. Isoda, *Microsc. Microanal.* **2009**, *15*, 106.
[74] A. A. Koroleva, A. G. Chernikova, A. A. Chouprik, E. S. Gornev, A. S. Slavich, R. R. Khakimov, E. V. Korostylev, C. S. Hwang, A. M. Markeev, *ACS Appl. Mater. Interfaces* **2020**, *12*, 55331.
[75] C. Charpin-Nicolle, M. Bonvalot, R. Sommer, A. Persico, M. L. Cordeau, S. Belahcen, B. Eychenne, P. Blaise, S. Martinie, S. Bernasconi, E. Jalaguier, E. Nowak, *Microelectron. Eng.* **2020**, *221*, 111194.
[76] M. Y. Zhuk, N. A. Sizykh, D. S. Kuzmichev, A. A. Chouprik, S. S. Zarubin, E. S. Gornev, A. V. Zenkevich, *ACS Appl. Nano. Mater.* **2022**, *5*, 8594.
[77] M. Sajedi Alvar, P. W. M. Blom, G.-J. A. H. Wetzelaer, *Nat. Commun.* **2020**, *11*, 4023.

[78] V. A. Cherepanov, A. R. Gilev, E. A. Kiselev, *Pure Appl. Chem.* **2019**, *91*, 911.
[79] L. Goux, A. Fantini, Y. Y. Chen, A. Redolfi, R. Degraeve, M. Jurczak, *ECS Solid State Lett.* **2014**, *3*, Q79.
[80] A. Rogalev, F. Wilhelm, *The Physics of Metals and Metallography* **2015**, *116*, 1285.
[81] R. J. Woolley, B. N. Illy, M. P. Ryan, S. J. Skinner, *J. Mater. Chem.* **2011**, *21*, 18592.